Letter | Editors' Suggestion

Site-Selective Quantum Control in an Isotopically Enriched $^{28}Si/Si_{0.7}Ge_{0.3}$ Quadruple Quantum Dot

A.J. Sigillito,[1] J.C. Loy,[1] D.M. Zajac,[1] M.J. Gullans,[1] L.F. Edge,[2] and J.R. Petta[1,*]

[1] *Department of Physics, Princeton University, Princeton, New Jersey 08544, USA*
[2] *HRL Laboratories LLC, 3011 Malibu Canyon Road, Malibu, California 90265, USA*

(Received 20 March 2019; published 26 June 2019)

Silicon spin qubits are a promising quantum-computing platform offering long coherence times, small device sizes, and compatibility with industry-backed device-fabrication techniques. In recent years, high-fidelity single-qubit and two-qubit operations have been demonstrated in Si. Here we demonstrate coherent spin control in a quadruple quantum dot fabricated from isotopically enriched ^{28}Si. We tune the ground-state charge configuration of the quadruple dot down to the single-electron regime and demonstrate tunable interdot tunnel couplings as large as 20 GHz, which enables exchange-based two-qubit gate operations. Site-selective single spin rotations are achieved with the use of electric dipole spin resonance in a magnetic field gradient. We execute a resonant controlled-NOT gate between two adjacent spins in 270 ns.

DOI: 10.1103/PhysRevApplied.11.061006

Quantum processors based on spins in semiconductors [1–3] are rapidly becoming a strong contender in the global race to build a quantum computer. In particular, silicon is an excellent host material for spin-based quantum computing by virtue of its weak spin-orbit coupling and low natural abundance of spin-carrying nuclei, which lead to intrinsically long spin coherence times [4,5]. Within the past few years, tremendous progress has been made in achieving high-fidelity single-qubit control [6,7] and two-qubit control [8–12] in silicon. Scalable one-dimensional arrays of silicon quantum dots have been demonstrated [13], and in GaAs, where electron wave functions are comparably large, both one-dimensional arrays [14–16] and two-dimensional arrays [17,18] of spins have been fabricated. Despite this progress, quantum control of spins in silicon has been limited to one- and two-qubit devices. Scaling beyond two-qubit devices opens the door to important experiments that are currently out of reach, including error correction [19,20], quantum simulation [21–24], and demonstrations of time-crystal phases [25].

In this letter, we demonstrate operation of a four-qubit device fabricated from an isotopically enriched $^{28}Si/Si_{0.7}Ge_{0.3}$ heterostructure. The device offers independent control of all four qubits, as well as pairwise two-qubit gates mediated by the exchange interaction [26]. We demonstrate control and measurement of the charge state of the array, and operate in the regime where each dot contains only one electron. We perform electric-dipole-spin-resonance (EDSR) spectroscopy on all four qubits to show that they have unique spin resonance frequencies. Finally, we modulate the tunnel coupling between adjacent dots and demonstrate a resonant controlled-NOT (CNOT) gate [9,27].

Four spin qubits are arranged in a linear array with use of an overlapping gate architecture, as shown in Fig. 1(a) [28]. Individual spin qubits are formed by accumulation of an electron under each plunger gate: P1, P2, P3, and P4. The couplings between dots and between dots and the charge reservoirs formed beneath gates S3 and D3 are tuned by adjustment of the barrier-gate voltages V_{Bi}. Charge sensing is performed by our monitoring the currents I_{S1} and I_{S2} through two proximal quantum-dot charge detectors located in the lower half of the device.

Charge-stability diagrams for the array are shown in Figs. 1(b) and 1(c). To obtain good charge sensitivity for all four dot charge transitions, $dI/dV = dI_{S1}/dV_{P1} + dI_{S1}/dV_{P4} + dI_{S2}/dV_{P1} + dI_{S2}/dV_{P4}$ is plotted as a function of V_{P1} and V_{P4}. In Fig. 1(b) we show that we can achieve the $(N_1, N_2, N_3, N_4) = (0, 0, 0, 0)$ charge state, where N_i denotes the number of electrons in dot i. The $(0, 0, 0, 0)$ charge state is evident from the large region devoid of charge transitions in the lower-left corner of Fig. 1(b). The device is typically operated in the (1,1,1,1) charge state, which is labeled in the enlarged charge-stability diagram in Fig. 1(c). The capacitive coupling between plunger gates and neighboring dots (i.e., gate P1 and dot 2) is naturally an order-of-magnitude weaker than the coupling between a plunger gate and the dot formed directly underneath it (i.e., gate P1 and dot 1) [28]. It can therefore be challenging to distinguish charge transitions in adjacent dots (P1 and P2, or P3 and P4) in two-dimensional

*petta@princeton.edu

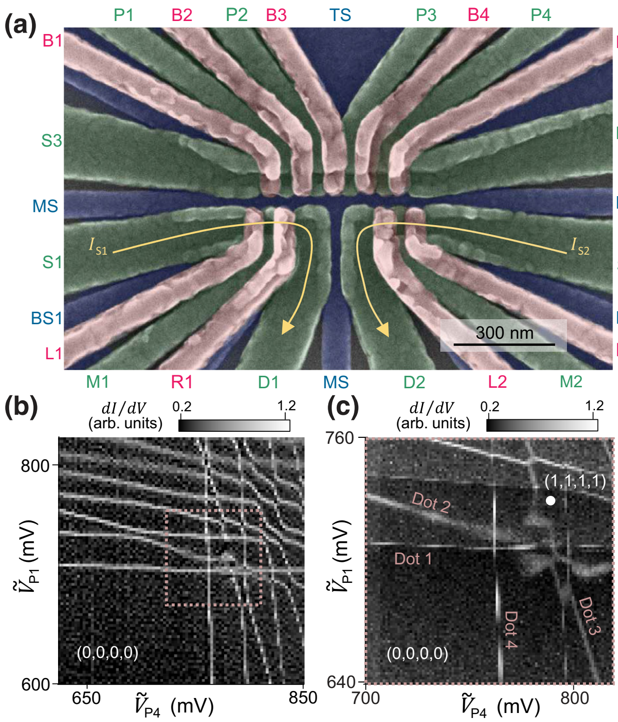

FIG. 1. (a) False-color scanning electron micrograph of the device. The qubit electrons are accumulated underneath the plunger gates P*i* and the charge-sensor dots are formed under the gates M*i*. (b) A large-scale charge-stability diagram shows that the array can be emptied of electrons to reach the (0,0,0,0) charge state. The sensing signal dI/dV is obtained by combining the differentiated signal from both charge detectors. (c) Charge-stability diagram acquired near the (1, 1, 1, 1) charge state, where quantum control is performed.

charge-stability plots since the slopes are very similar. To more clearly distinguish the charge transitions, an artificial cross-coupling is added between each plunger gate and its neighboring plunger gates in software (details are available in Supplemental Material [29]) such that a sweep in $V_{\rm P1}$ and $V_{\rm P4}$ induces transitions not only in dots 1 and 4 but also in dots 2 and 3. To distinguish when the artificial coupling is used, we relabel $V_{\rm P1}$ and $V_{\rm P4}$ as $\tilde{V}_{\rm P1}$ and $\tilde{V}_{\rm P4}$, respectively. With the (1,1,1,1) charge state having been identified, we next establish virtual gates, which significantly streamline device tuning.

Virtual gates have been described in detail and compensate for the effects of device cross-capacitance through software corrections that effectively invert the capacitance matrix [21,30–33]. Whenever the voltage of gate $V_{{\rm P}i}$ is adjusted to tune the chemical potential of dot i, the voltages on adjacent gates $V_{{\rm P}(i-1)}$ and $V_{{\rm P}(i+1)}$ are modified by a calibrated amount to keep the chemical potentials of dots $i-1$ and $i+1$ constant. The measured capacitance matrix is given in Supplemental Material [29] and is used to establish the virtual-gate space [30].

Pairwise charge-stability diagrams measured with virtual gates are shown in Figs. 2(a)–2(c). As the two virtual gates u_i and u_{i+1} are swept, the charge-sensor currents $I_{\rm S1}$ and $I_{\rm S2}$ are measured. Here we plot $I_{\rm S1} - I_{\rm S2}$ as it results in higher charge-sensing contrast. Gates not being swept [i.e., u_3 and u_4 in Fig. 2(a)] are held fixed at the same chemical potential as the source and drain reservoirs to enable fast loading and unloading of electrons throughout the array. The orthogonality of the charge transitions indicates that we have independent control of each quantum dot's chemical potential.

Loss and DiVincenzo [1] suggested that the exchange interaction between two spins could be modulated by adjustment of the height of the tunnel barrier separating the spins. We demonstrate control over all of the interdot tunnel couplings (t_{cij}) in our device by measuring the charge-state occupation as a function of detuning ϵ_{ij} for different barrier-gate voltages $V_{{\rm B}i}$. In Fig. 2(d) $P_{(0,1,*,*)}$ is plotted along the detuning axis shown in Fig. 2(a). The asterisk denotes that the chemical potential of the dot is

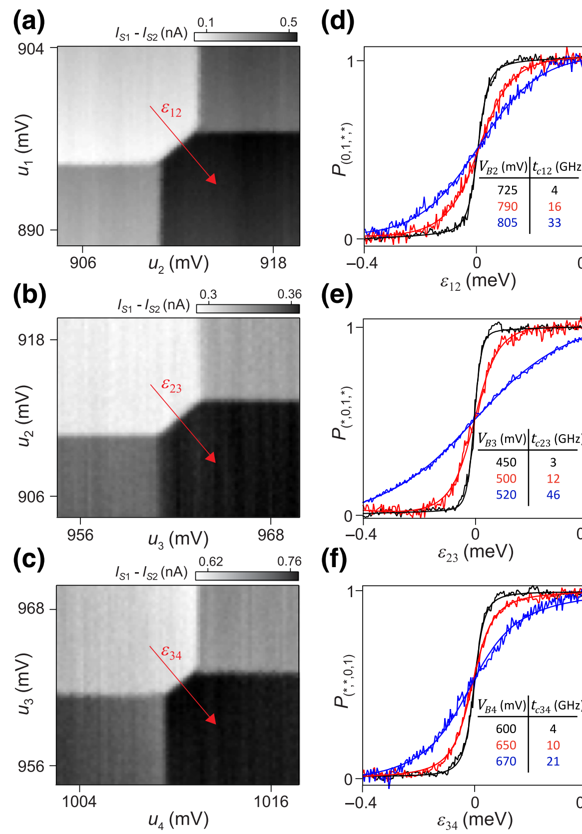

FIG. 2. Pairwise charge-stability diagrams measured for (a) dots 1 and 2, (b) dots 2 and 3, and (c) dots 3 and 4. Here we use virtual gates to independently tune each dot's chemical potential. (d)–(f) Charge-state occupation measured as a function of detuning ϵ_{ij} for various barrier-gate voltages $V_{{\rm B}i}$. An increase in interdot tunnel coupling broadens the interdot charge transitions. The data are fit to theoretical predictions (solid lines) to extract the interdot tunnel coupling t_{cij} between dots i and j [34].

TABLE I. Summary of single-qubit parameters, including lever-arm conversion between gate voltage and energy α, charging energy E_c, magnetic field offset due to the micromagnet B_i^M, spin dephasing time T_2^*, and spin coherence time $T_{2,\text{echo}}$.

Dot	α (meV/mV)	E_c (meV)	B_i^M (mT)	T_2^* (μs)	$T_{2,\text{echo}}$ (μs)
1	0.14	4.5	137.6	2.6	41
2	0.13	4.7	165.8	1.5	31
3	0.14	4.5	194.3	10.4	72
4	0.15	4.7	199.2	9.4	109

held at the same value as the source and drain chemical potentials. As the tunnel coupling is increased, the charge delocalizes across adjacent dots and the interdot charge transition broadens. These data are fit as described in Refs. [34,35] to extract the interdot tunnel coupling. The lever-arm conversion between gate voltage and energy is determined by measuring finite-bias triangles for each pair of dots as reported in Table I. As shown by the data, the device offers a high degree of control, with tunnel coupling tunable from $2t_{cij} \approx k_B T_e \approx 2$ GHz to many tens of gigahertz, which is sufficient to enable fast CNOT gates. Here k_B is Boltzmann's constant, and the electron temperature $T_e \approx 90$ mK is obtained by fitting the charge transitions to the source and drain to a Fermi function as described in Ref. [13].

Site-selective single spin rotations are achieved with use of EDSR [36,37] in the presence of a magnetic field gradient generated by a Co micromagnet [29]. The field from the micromagnet B_i^M is different at each dot and therefore each spin has a unique ESR frequency f_i given by $hf_i = g\mu_B(B_{\text{ext}} + B_i^M)$, where h is Planck's constant, $g \approx 2$ is the Landé g factor, and B_{ext} is the externally applied magnetic field. Our micromagnet design is similar to that used by Yoneda *et al.* [38], but it has a slanting edge (as seen from above) that extends the field gradient over the entire quadruple quantum dot [29].

To map out B_i^M, EDSR spectroscopy is performed on each qubit. During spectroscopy, the array is configured such that only dot i contains a single electron (all other dots are empty). In practice, we find that adding an electron to an adjacent dot shifts the resonance frequency by only a few megahertz. A frequency-chirped microwave pulse (± 15 MHz around a frequency f for 120 μs) is applied to gate MS. If the chirped pulse sweeps through the spin resonance frequency f_i of dot i, its spin will end up in a mixed state. Here our chirped pulses are not adiabatic, but are nonetheless convenient for identifying spin resonance conditions, as the linewidth of electron spins in ^{28}Si can be narrow (less than 100 kHz). The spin state of dot i is then measured through spin-selective tunneling to the leads [39]. In the case of $i = 2$ and $i = 3$, where the dots are not directly connected to the leads, the electron is shuttled to the edge of the array and read out in dot 1 or dot 4, respectively. Loading the array follows the read-out sequence in reverse. These measurements are repeated over a B_{ext} range from 250 to 450 mT.

The spectra for all four qubits are summed and plotted in Fig. 3(a). The field gradient from the micromagnet separates the qubit resonance frequencies by hundreds of megahertz, as highlighted by the line-cut through the data in Fig. 3(b). For comparison, in silicon devices relying on Stark shifts or interface disorder for spin selectivity, the qubit splitting is typically a few tens of megahertz [5,8,11]. We find that over the course of approximately 24 h the qubit frequencies are constant to within a few hundred kilohertz. The read-out visibility is primarily limited by T_e and spin relaxation ($T_1 = 52$ ms for qubit 4). The latter can be overcome by use of cryogenic current amplifiers to reduce noise and increase the measurement bandwidth [40].

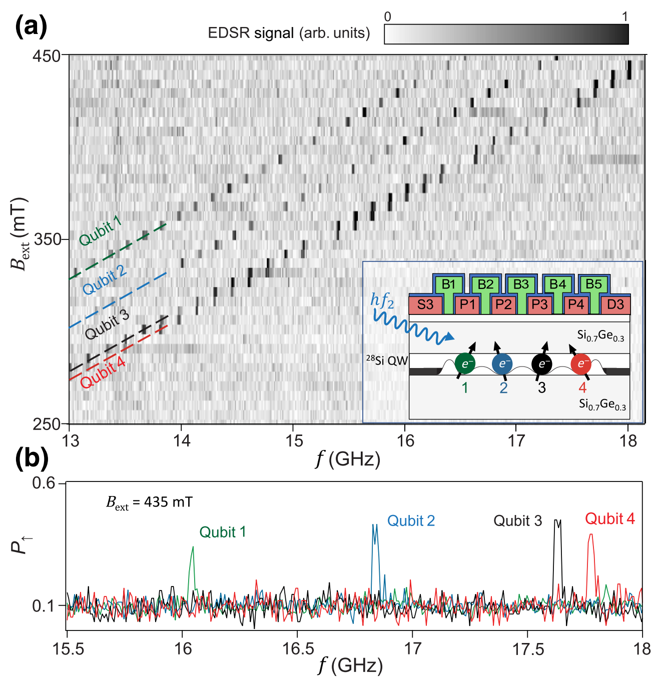

FIG. 3. (a) Summed EDSR spectra for all four qubits. The qubits are driven with use of gate MS, and four distinct ESR transitions are observed. The ESR lines do not appear continuous due to undersampling in B_{ext}. The inset shows a cross-section cartoon of the device showing all four qubits subjected to the same driving field, but with only qubit 2 in resonance. (b) A line-cut through the data at $B_{\text{ext}} = 435$ mT shows that all four qubits are well separated in frequency. The spacing between qubits 1, 2, and 3 is approximately 800 MHz, and qubits 3 and 4 are separated by approximately 130 MHz. The qubit linewidths are broadened by the 30-MHz microwave chirp used in these measurements.

We next measure the spin dephasing times T_2^* and spin coherence times T_2 for each qubit (see Table I). In natural silicon, spin coherence is limited by the hyperfine interaction with the 4.7%-abundance ^{29}Si nuclei. Here our device consists of an isotopically enriched ^{28}Si quantum well (QW), which is 4.9 nm thick and has only an 800-ppm residual concentration of ^{29}Si [41,42]. The buffer layers, however, consist of natural Si and natural Ge containing residual spin-1/2 and spin-9/2 nuclei, respectively. Wave-function overlap with these nuclei will be non-negligible given the relatively thin QW [43].

T_2^* is determined through measurements of Ramsey fringes. For each Ramsey decay curve, the data are integrated over 15 min. Qubits 3 and 4 show a nearly tenfold increase in T_2^* compared with $T_2^* \sim 1\ \mu$s for electron spins in natural silicon, whereas qubits 1 and 2 have a dephasing time that is comparable to that of natural silicon. A simple Hahn-echo pulse sequence significantly extends the coherence times, as summarized in Table I. Similar fluctuations in the coherence times have been observed in other devices [9–11] and may be due to sampling over a relatively small number of spin-carrying nuclei in the QW and $Si_{0.7}Ge_{0.3}$ barrier layers. Another reason for the fast dephasing in qubits 1 and 2 could be charge noise, which has been shown to reduce T_1 [44] and T_2 [6] in the presence of field gradients and is discussed in Supplemental Material [29]. Because of the wedge-shaped geometry of the micromagnet, the field gradient experienced by qubits 1 and 2 is significantly larger than at sites 3 and 4, which is evident from the large change in field offsets B_i^M between dots 1, 2, and 3, and a relatively small change in B_i^M between dots 3 and 4 (see Table I). The short coherence times in dots 1 and 2 are still comparable with the times reported in natural Si QWs and are not prohibitive for two-qubit operation.

To perform two-qubit gates, we apply voltage pulses to the barrier gates Bi separating the dots [1]. Applying a positive voltage to a barrier gate increases wave-function overlap between adjacent dots and turns on exchange [27], as illustrated in the energy-level diagram in Fig. 4(a). To first map out the influence of the barrier gate on the exchange interaction, we vary the gate voltage V_{B4} and perform EDSR spectroscopy on qubit 3 [see Fig. 4(b)]. Before we measure the EDSR spectrum of qubit 3, qubit 4 is prepared in a mixed state such that any state-dependent line splitting can be observed [9]. The EDSR spectrum of qubit 4 is probed in a similar way. As V_{B4} is increased, the EDSR lines split to reveal a doublet with a peak separation that is equal to the exchange energy J_{34}. The overall frequency shift of the doublet is attributed to the displacement of the electron's wave function within the magnetic field gradient as V_{B4} is adjusted [9]. When voltage pulses are applied to any gates, these induced frequency shifts must be accounted for and corrected with use of single-qubit z rotations [9,45].

A resonant CNOT gate can be achieved with this device architecture by following the protocol developed by Zajac *et al.* [9]. Here we focus on qubits 3 and 4, while dots

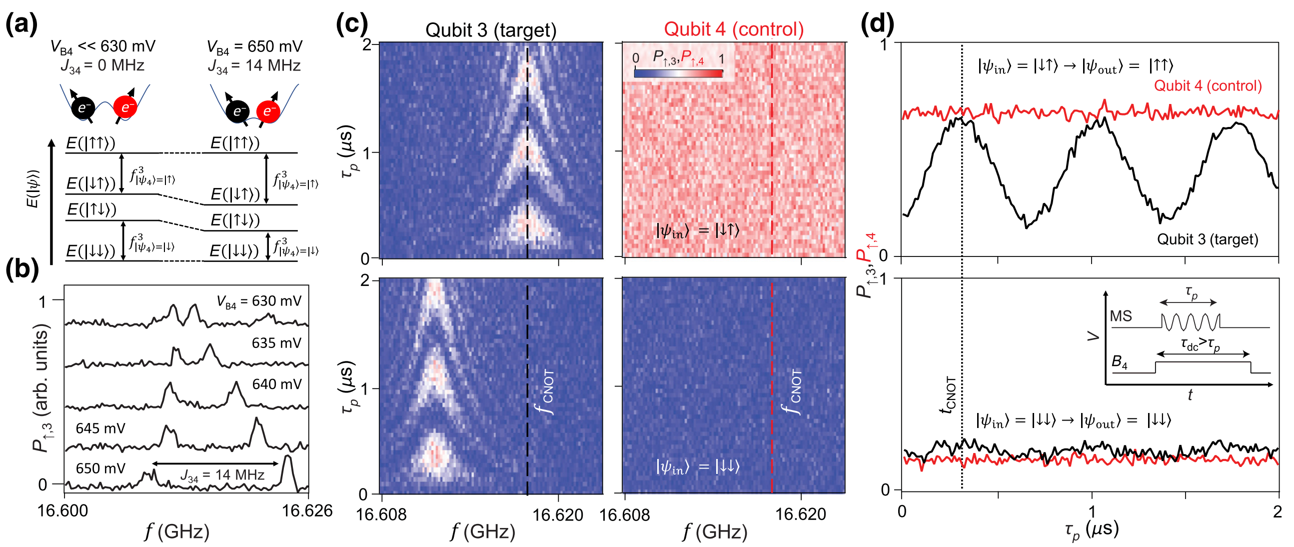

FIG. 4. (a) Energy-level diagram for dots 3 and 4 subjected to a magnetic field gradient and either no exchange (left) or finite exchange (right). Increasing V_{B4} turns on the exchange interaction J_{34} between qubits 3 and 4. Under exchange, the spin transition frequency of qubit 3 (the target qubit) $f^{(3)}$ depends on the input state of qubit 4 $|\Psi_4\rangle$ (the control qubit). (b) EDSR spectra of qubit 3. The spin-up probability $P_{\uparrow,3}$ is plotted as a function of f and V_{B4}. (c) By varying the frequency and amplitude of a microwave pulse applied to the target qubit with the control qubit prepared in either the up state (top panels) or the down state (bottom panels), we map out the frequency of the target qubit conditioned on the state of the control qubit. (d) Driving at frequency f_{CNOT} and varying the microwave burst time τ_p results in Rabi oscillations of the target qubit that are conditioned on the state of the control qubit. When the microwave burst is timed to correspond to a π rotation on the target qubit, $\tau_p = \tau_{CNOT} = 270$ ns, a CNOT gate is achieved (dotted line).

1 and 2 are empty. With $J_{34} \approx 0$, we prepare input state $|\psi_{\rm in}\rangle = |\downarrow\downarrow\rangle$ through spin-selective tunneling or input state $|\psi_{\rm in}\rangle = |\downarrow\uparrow\rangle$ through spin-selective tunneling followed by a π pulse on spin 4. We then apply a voltage pulse to gate B4 to turn on exchange while simultaneously applying a microwave burst of varying duration τ_p and frequency f. The resulting spin-up probabilities $P_{\uparrow,3}$ ($P_{\uparrow,4}$) for qubit 3 (4) are plotted in Fig. 4(c). Rabi oscillations are observed for qubit 3 with a resonance frequency that is dependent on the state of qubit 4. By setting $f = f_{\rm CNOT}$, where the microwave tone is resonant with the target qubit when the control qubit is in the spin-up state, we drive Rabi oscillations on the target qubit conditioned on the state of the control qubit [see Fig. 4(d)]. Furthermore, when $t = t_{\rm CNOT}$, qubit 3 will be flipped when qubit 4 is in the spin-up state. With these settings, we realize a resonant CNOT gate in a four-qubit device [9,27]. To implement a high-fidelity CNOT gate, it is important to note that some additional phase accumulation due to the $V_{\rm B4}$-induced Ising interaction must be compensated for by proper tuning of $\tau_{\rm dc}$ and $V_{\rm B4}$ as described in our previous work [9,27]. We attribute the slight oscillations that appear on qubit 3 in the lower panel in Fig. 4(d) to state-preparation errors on qubit 4. Off-resonant driving would lead to oscillations at a frequency above 6 MHz.

In conclusion, we demonstrate one- and two-qubit gate operations in a four-qubit device fabricated from an isotopically enriched ^{28}Si QW. Our device design allows full control of the charge state in the array. Interdot tunnel coupling and exchange are tuned with use of barrier gates. We demonstrate independent control of all four qubits, which is enabled by the field gradient from a Co micromagnet. To demonstrate a two-qubit gate involving dots 3 and 4, we map exchange as a function of $V_{\rm B4}$ and perform a resonant CNOT gate in 270 ns. These results set the stage for a four-qubit spin-based quantum processor in silicon, which should be capable of performing small-scale quantum algorithms and demonstrating time-crystal phases [25].

ACKNOWLEDGMENTS

This work was funded by Army Research Office Grant No. W911NF-15-1-0149, DARPA Grant No. D18AC0025, and the Gordon and Betty Moore Foundation's EPiQS Initiative through Grant No. GBMF4535. Devices were fabricated in the Princeton University Quantum Device Nanofabrication Laboratory. The authors acknowledge the use of Princeton University's Imaging and Analysis Center, which is partially supported by the Princeton Center for Complex Materials, a National Science Foundation Materials Research Science and Engineering Center (Grant No. DMR-1420541).

[1] D. Loss and D. P. DiVincenzo, Quantum computation with quantum dots, Phys. Rev. A **57**, 120 (1998).

[2] R. Hanson, L. P. Kouwenhoven, J. R. Petta, S. Tarucha, and L. M. K. Vandersypen, Spins in few-electron quantum dots, Rev. Mod. Phys. **79**, 1217 (2007).

[3] F. A. Zwanenburg, A. S. Dzurak, A. Morello, M. Y. Simmons, L. C. L. Hollenberg, G. Klimeck, S. Rogge, S. N. Coppersmith, and M. A. Eriksson, Silicon quantum electronics, Rev. Mod. Phys. **85**, 961 (2013).

[4] A. M. Tyryshkin, S. Tojo, J. J. L. Morton, H. Riemann, N. V. Abrosimov, P. Becker, H.-J. Pohl, T. Schenkel, M. L. W. Thewalt, K. M. Itoh, and S. A. Lyon, Electron spin coherence exceeding seconds in high-purity silicon, Nat. Mater. **11**, 143 (2012).

[5] M. Veldhorst, J. C. C. Hwang, C. H. Yang, A. W. Leenstra, B. De Ronde, J. P. Dehollain, J. T. Muhonen, F. E. Hudson, K. M. Itoh, A. Morello, and A. S. Dzurak, An addressable quantum dot qubit with fault-tolerant control-fidelity, Nat. Nanotechnol. **9**, 981 (2014).

[6] J. Yoneda, K. Takeda, T. Otsuka, T. Nakajima, M. R. Delbecq, G. Allison, T. Honda, T. Kodera, S. Oda, Y. Hoshi, N. Usami, K. M. Itoh, and S. Tarucha, A quantum-dot spin qubit with coherence limited by charge noise and fidelity higher than 99.9%, Nat. Nanotechnol. **13**, 102 (2018).

[7] C. H. Yang, K. W. Chan, R. Harper, W. Huang, T. Evans, J. C. C. Hwang, B. Hensen, A. Laucht, T. Tanttu, F. E. Hudson, S. T. Flammia, K. M. Itoh, A. Morello, S. D. Bartlett, and A. S. Dzurak, Silicon qubit fidelities approaching incoherent noise limits via pulse optimisation, Nat. Electron. **2**, 151 (2019).

[8] M. Veldhorst, C. H. Yang, J. C. C. Hwang, W. Huang, J. P. Dehollain, J. T. Muhonen, S. Simmons, A. Laucht, F. E. Hudson, K. M. Itoh, A. Morello, and A. S. Dzurak, A two-qubit logic gate in silicon, Nature **526**, 410 (2015).

[9] D. M. Zajac, A. J. Sigillito, M. Russ, F. Borjans, J. M. Taylor, G. Burkard, and J. R. Petta, Resonantly driven CNOT gate for electron spins, Science **359**, 439 (2018).

[10] T. F. Watson, S. G. J. Philips, E. Kawakami, D. R. Ward, P. Scarlino, M. Veldhorst, D. E. Savage, M. G. Lagally, M. Friesen, S. N. Coppersmith, M. A. Eriksson, and L. M. K. Vandersypen, A programmable two-qubit quantum processor in silicon, Nature **555**, 633 (2018).

[11] W. Huang, C. H. Yang, K. W. Chan, T. Tanttu, B. Hensen, R. C. C. Leon, M. A. Fogarty, J. C. C. Hwang, F. E. Hudson, K. M. Itoh, A. Morello, A. Laucht, and A. S. Dzurak, Fidelity benchmarks for two-qubit gates in silicon, Nature **569**, 532 (2019).

[12] X. Xue, T. F. Watson, J. Helsen, D. R. Ward, D. E. Savage, M. G. Lagally, S. N. Coppersmith, M. A. Eriksson, S. Wehner, and L. M. K. Vandersypen, Benchmarking Gate Fidelities in a Si/SiGe Two-Qubit Device, Phys. Rev. X **9**, 021011 (2019).

[13] D. M. Zajac, T. M. Hazard, X. Mi, E. Nielsen, and J. R. Petta, Scalable Gate Architecture for a One-Dimensional Array of Semiconductor Spin Qubits, Phys. Rev. Appl. **6**, 054013 (2016).

[14] A. Noiri, J. Yoneda, T. Nakajima, T. Otsuka, M. R. Delbecq, K. Takeda, S. Amaha, G. Allison, A. Ludwig, A. D. Wieck, and S. Tarucha, Coherent electron-spin-resonance manipulation of three individual spins in a triple quantum dot, Appl. Phys. Lett. **108**, 153101 (2016).

[15] T. Otsuka, T. Nakajima, M. R. Delbecq, S. Amaha, J. Yoneda, K. Takeda, G. Allison, T. Ito, R. Sugawara, A.

Noiri, A. Ludwig, A. D. Wieck, and S. Tarucha, Single-electron spin resonance in a quadruple quantum dot, Sci. Rep. **6**, 31820 (2016).

[16] T. Ito, T. Otsuka, T. Nakajima, M. R. Delbecq, S. Amaha, J. Yoneda, K. Takeda, A. Noiri, G. Allison, A. Ludwig, A. D. Wieck, and S. Tarucha, Four single-spin Rabi oscillations in a quadruple quantum dot, Appl. Phys. Lett. **113**, 093102 (2018).

[17] P.-A. Mortemousque, E. Chanrion, B. Jadot, H. Flentje, A. Ludwig, A. D. Wieck, M. Urdampilleta, C. Bauerle, and T. Meunier, Coherent control of individual electron spins in a two dimensional array of quantum dots, arXiv:1808.06180 (2018).

[18] U. Mukhopadhyay, J. P. Dehollain, C. Reichl, W. Wegscheider, and L. M. K. Vandersypen, A 2×2 quantum dot array with controllable inter-dot tunnel couplings, Appl. Phys. Lett. **112**, 183505 (2018).

[19] M. D. Reed, L. DiCarlo, S. E. Nigg, L. Sun, L. Frunzio, S. M. Girvin, and R. J. Schoelkopf, Realization of three-qubit quantum error correction with superconducting circuits, Nature **482**, 382 (2012).

[20] P. Schindler, J. T. Barreiro, T. Monz, V. Nebendahl, D. Nigg, M. Chwalla, M. Hennrich, and R. Blatt, Experimental repetitive quantum error correction, Science **332**, 1059 (2011).

[21] T. Hensgens, T. Fujita, L. Janssen, X. Li, C. J. van Diepen, C. Reichl, W. Wegscheider, S. Das Sarma, and L. M. K. Vandersypen, Quantum simulation of a Fermi-Hubbard model using a semiconductor quantum dot array, Nature **548**, 70 (2017).

[22] I. M. Georgescu, S. Ashhab, and F. Nori, Quantum simulation, Rev. Mod. Phys. **86**, 153 (2014).

[23] P. Barthelemy and L. M. K. Vandersypen, Quantum dot systems: A versatile platform for quantum simulations, Ann. Phys. **525**, 808 (2013).

[24] T. Byrnes, N. Y. Kim, K. Kusudo, and Y. Yamamoto, Quantum simulation of Fermi-Hubbard models in semiconductor quantum-dot arrays, Phys. Rev. B **78**, 075320 (2008).

[25] E. Barnes, J. M. Nichol, and S. E. Economou, Stabilization and manipulation of multispin states in quantum-dot time crystals with Heisenberg interactions, Phys. Rev. B **99**, 035311 (2019).

[26] J. R. Petta, A. C. Johnson, J. M. Taylor, E. A. Laird, A. Yacoby, M. D. Lukin, C. M. Marcus, M. P. Hanson, and A. C. Gossard, Coherent manipulation of coupled electron spins in semiconductor quantum dots, Science **309**, 2180 (2005).

[27] M. Russ, D. M. Zajac, A. J. Sigillito, F. Borjans, J. M. Taylor, J. R. Petta, and G. Burkard, High-fidelity quantum gates in Si/SiGe double quantum dots, Phys. Rev. B **97**, 085421 (2018).

[28] D. M. Zajac, T. M. Hazard, X. Mi, K. Wang, and J. R. Petta, A reconfigurable gate architecture for Si/SiGe quantum dots, Appl. Phys. Lett. **106**, 223507 (2015).

[29] See Supplemental Material at http://link.aps.org/supplemental/10.1103/PhysRevApplied.11.061006 for additional device-characterization data.

[30] A. R. Mills, D. M. Zajac, M. J. Gullans, F. J. Schupp, T. M. Hazard, and J. R. Petta, Shuttling a single charge across a one-dimensional array of silicon quantum dots, Nat. Commun. **10**, 1063 (2019).

[31] T. A. Baart, M. Shafiei, T. Fujita, C. Reichl, W. Wegscheider, and L. M. K. Vandersypen, Single-spin CCD, Nat. Nanotechnol. **11**, 330 (2016).

[32] C. J. van Diepen, P. T. Eendebak, B. T. Buijtendorp, U. Mukhopadhyay, T. Fujita, C. Reichl, W. Wegscheider, and L. M. K. Vandersypen, Automated tuning of inter-dot tunnel coupling in double quantum dots, Appl. Phys. Lett. **113**, 033101 (2018).

[33] C. Volk, A. M. J. Zwerver, U. Mukhopadhyay, P. T. Eendebak, C. J. van Diepen, J. P. Dehollain, T. Hensgens, T. Fujita, C. Reichl, W. Wegscheider, and L. M. K. Vandersypen, Loading a quantum-dot based “qubyte” register, npj Quantum Inf. **5**, 29 (2019).

[34] L. DiCarlo, H. J. Lynch, A. C. Johnson, L. I. Childress, K. Crockett, C. M. Marcus, M. P. Hanson, and A. C. Gossard, Differential Charge Sensing and Charge Delocalization in a Tunable Double Quantum Dot, Phys. Rev. Lett. **92**, 226801 (2004).

[35] J. R. Petta, A. C. Johnson, C. M. Marcus, M. P. Hanson, and A. C. Gossard, Manipulation of a Single Charge in a Double Quantum Dot, Phys. Rev. Lett. **93**, 186802 (2004).

[36] M. Pioro-Ladriere, T. Obata, Y. Tokura, Y.-S. Shin, T. Kubo, K. Yoshida, T. Taniyama, and S. Tarucha, Electrically driven single-electron spin resonance in a slanting Zeeman field, Nat. Phys. **4**, 776 (2008).

[37] Y. Tokura, W. G. van der Wiel, T. Obata, and S. Tarucha, Coherent Single Electron Spin Control in a Slanting Zeeman Field, Phys. Rev. Lett. **96**, 047202 (2006).

[38] J. Yoneda, T. Otsuka, T. Takakura, M. Pioro-Ladrière, R. Brunner, H. Lu, T. Nakajima, T. Obata, A. Noiri, C. J. Palmstrøm, A. C. Gossard, and S. Tarucha, Robust micromagnet design for fast electrical manipulations of single spins in quantum dots, APEX **8**, 084401 (2015).

[39] J. M. Elzerman, R. Hanson, L. H. W. Van Beveren, B. Witkamp, L. M. K. Vandersypen, and L. P. Kouwenhoven, Single-shot read-out of an individual electron spin in a quantum dot, Nature **430**, 431 (2004).

[40] I. T. Vink, T. Nooitgedagt, R. N. Schouten, L. M. K. Vandersypen, and W. Wegscheider, Cryogenic amplifier for fast real-time detection of single-electron tunneling, Appl. Phys. Lett. **91**, 123512 (2007).

[41] P. W. Deelman, L. F. Edge, and C. A. Jackson, Metamorphic materials for quantum computing, Mater. Res. Bull. **41**, 224 (2016).

[42] C. J. K. Richardson, C. A. Jackson, L. F. Edge, and P. W. Deelman, High-resolution x-ray reflection Fourier analysis of metamorphic Si/SiGe quantum wells, J. Vac. Sci. Technol. B **35**, 02B113 (2017).

[43] W. M. Witzel, M. S. Carroll, L. Cywiński, and S. Das Sarma, Quantum decoherence of the central spin in a sparse system of dipolar coupled spins, Phys. Rev. B **86**, 035452 (2012).

[44] F. Borjans, D. Zajac, T. Hazard, and J. Petta, Single-Spin Relaxation in a Synthetic Spin-Orbit Field, Phys. Rev. Appl. **11**, 044063 (2019).

[45] K. Takeda, J. Yoneda, T. Otsuka, T. Nakajima, M. Delbecq, G. Allison, Y. Hoshi, N. Usami, K. Itoh, S. Oda, T. Kodera, and S. Tarucha, Optimized electrical control of a Si/SiGe spin qubit in the presence of an induced frequency shift, npj Quantum Inf. **4**, 54 (2018).